Entangled core/shell magnetic structure driven by surface magnetic symmetry-breaking in Cr_2O_3 nanoparticles

Natalia Rinaldi-Montes,[a] Pedro Gorria,*[b] Antonio B. Fuertes,[c] David Martínez-Blanco,[d] Zakariae Amghouz,[e] Inés Puente-Orench,[f] Luca Olivi,[g] Javier Herrero-Martín,[h] M. P. Fernández-García,[a] Javier Alonso,[i] Manh-Huong Phan,[j] Hariharan Srikanth,[j] Xavi Marti [k] and Jesús A. Blanco[a]

Bulk Cr_2O_3 is an antiferromagnetic (AFM) oxide that exhibits the magnetoelectric effect at room temperature, with neither spontaneous magnetization nor net electric polarization. These physical properties stem from a subtle competition between exchange and crystal field interactions. In this article, we exploit the symmetry breaking at the surface of Cr_2O_3 nanoparticles for unbalancing this delicate physical equilibrium. The emerging weak ferromagnetic signal we observe persists up to near room temperature ($\approx$ 270 K) at which the antiferromagnetic order disappears. In addition, an exchange-bias effect, that rapdily falls down on heating from low temperature up to 30 K, is resistant to thermal disorder above 200 K. Our findings point to the possible formation of an entangled core/shell magnetic structure, where pinned uncompensated spins at the shell are randomly distributed in a low-temperature spin-glass ordering, with low net magnetic moment and an ordering temperature governed by the AFM Néel temperature.

Introduction

More than eight decades after Louis Néel first elucidated the phenomenon of magnetic nanoparticles (NPs) [1], the activity in investigating their magnetic properties is still the subject of intense research and progress. This interest is mainly motivated by the large variety of physical and chemical phenomena, and their potential perspective for applications in health [2], spintronics [3] or environmental areas [4] among others. Most of the success has been possible due to the combination of two main features; first, the development and improvement of synthesis methods that enable the preparation of NPs with very high reproducibility; and the access to more powerful experimental techniques that allow characterizing the individual NPs down to sub-nanometre resolution, being selective to the element, energy, and valence of the constituents of the NPs.

In recent years, the striking resurgence of interest in antiferromagnetic (AFM) magnetoelectric materials has been fuelled by the demand of electric control in non-volatile magnetic memory and logic applications [5-8]. These systems are particularly appealing due to the coupling between the magnetic and the electric properties of a material [9-12]. From a broader perspective, Cr_2O_3 is a better suited material for spin current from sub-terahertz-generated AFM magnons [13], catalysis [14, 15], bio-nanotechnology [16] or nuclear radiation [17].

Cr_2O_3 NPs turn out to be an excellent test bed for investigating the appearance of new phenomena [12, 18, 19]. The super-exchange interactions responsible for the AFM ground state in Cr_2O_3 arise from the existence of tight positive and negative magnetic competing interactions [20]. NPs possess a very large surface area where structural modifications are likely present [21-24]. By this token, minimal unit cell distortions, as expected at the NP boundaries, might encompass the switching between ferromagnetic (FM) and AFM long range orders akin to the achievement of a net FM contribution in Cr_2O_3 thin films [25, 26]. Similarly, size reduction down to the nanometer length-scale could give rise to low-temperature spin-glass behaviour and a large FM signal in an archetypical antiferromagnet like NiO [27-29].

The Cr_2O_3 NPs we have synthesized exhibit unexpected exchange bias coupling up to ~ 270 K due to the successful modification of the original AFM structure, leading to a more complex magnetic arrangement across the NPs. This possibility was suggested by a theoretical prediction some years ago [12]. In addition, our compelling experimental evidence suggests that the complex magnetic arrangement is located at a thin 2 nm outer shell of the NPs in which a reduced Cr coordination is detected.

Experimental methods

Synthesis of nanoparticles

The Cr_2O_3 nanoparticles were prepared following a similar silica gel template-assisted procedure previously reported [30]. In a typical synthesis (see panels a & b in Fig. 1), hydrated chromium nitrate, $Cr(NO_3)_3$ $9H_2O$, was dissolved in ethanol (around 0.8 g-nitrate/g-ethanol). Afterwards, the silica gel (SiO_2, Aldrich, Ref. 391484) was impregnated with this solution until incipient wetness was attained. The impregnated sample was vacuum-dried at 55° C. The impregnation-drying cycle was repeated up to three times for a high loading of the chromium nitrate into

[a.] Departamento de Física, Universidad de Oviedo, E-33007 Oviedo, Spain.
[b.] Departamento de Física & IUTA, EPI, Universidad de Oviedo, E-33203 Gijón, Spain.
[c.] Instituto Nacional del Carbón (CSIC), E-33080 Oviedo, Spain.
[d.] Servicios Científico-Técnicos, Universidad de Oviedo, E-33006 Oviedo, Spain.
[e.] Departamento de Ciencia de Materiales e Ingeniería Metalúrgica, Universidad de Oviedo, E-33004 Oviedo, Spain.
[f.] Instituto de Ciencia de Materiales de Aragón, CSIC-Universidad de Zaragoza and Institut Laue-Langevin, BP 156, F-38042 Grenoble Cedex 9, France.
[g.] Elettra-Sincrotrone Trieste S.C.p.A., 34149 Basovizza, Trieste, Italy.
[h.] ALBA Synchrotron, 08290 Cerdanyola del Vallès, Barcelona, Spain.
[i.] CITIMAC, Facultad de Ciencias, Universidad de Cantabria, E-39005, Santander, Spain.
[j.] Department of Physics, University of South Florida, FL 33620, Tampa, USA.
[k.] Institute of Physics, Czech Academy of Sciences, Cukrovarnická 10, 162 53, Prague 6, Czech Republic.

the silica porosity. The resulting sample was then calcined in air at 400° C (3° C/min) for 4 hours. The Cr_2O_3 products were obtained after dissolution of the silica template in a 2M NaOH solution. The subsequent sample was washed several times with distilled water until no traces of Si were detected by energy-dispersive x-ray (EDX) spectroscopy. After the NaOH etching procedure blackberry-shaped Cr_2O_3 powders are produced (see panel c in Fig. 1) that are formed by agglomeration of numerous single-domain NPs (see panel d in Fig. 1). The powders have mean diameter below the micron, with a distribution of sizes that seems to be an inverse replica of the template porosity. However, despite the presence of agglomeration in the powders, a meticulous study on a considerable number of HRTEM images has allowed us to extract information on the size distribution of each of the monodomain Cr_2O_3NPs, finding that on average the mean size is around 17 nm with a standard deviation of 3 nm (see panel f in Fig. 1). The standard polycrystalline bulk Cr_2O_3 used for comparison throughout the article was purchased from Alfa Aesar (Puratronic®, 99.97% metals basis).

Characterization techniques

Scanning electron microscopy (SEM) micrographs were recorded under a FEI Quanta FEG650 scanning electron microscope. HRTEM images and selected-area electron diffraction (SAED) patterns were obtained using a JEOL-JEM-2100F microscope operating at 200 kV. X-ray diffraction (XRD) patterns were collected by means of a Seifert XDR 3000 T/T diffractometer with Mo Kα1 (0.709316 Å) and Kα2 (0.713607 Å) radiations. The measurements were carried out in an angular range of 5-55° in steps of 0.03° and a collection time of 30 s. A standard LaB$_6$ sample was used for instrumental resolution. The full profile fitting of the XRD patterns was performed using the FullProf suite package [31] based on the Rietveld method [32], with rather good reliability factors, $i.e.$, the R-weighted pattern (R_{wp}) being below 5%.

Cr K-edge x-ray absorption (XAS) spectra were collected on the XAS beamline (BL 11.1R) at Elettra Synchrotron (Trieste, Italy). Pellets made of a mixture of boron nitride and Cr_2O_3 samples were compacted in a hydraulic press. The amount of the powdered sample was optimized to get a good signal-to-noise ratio. The spectra were measured in transmission mode at 77 K up to k = 20 Å^{-1} using standard ionization chambers. A metallic Cr-foil spectrum was recorded simultaneously to calibrate the energy. The extended x-ray absorption fine structure (EXAFS) signals were extracted from each spectra using conventional procedures for background subtraction and data normalization as implemented in the Athena software from IFEFFIT package [33].

Then, the EXAFS signal (in the energy range from 25 to 1600 eV above the edge) was converted to photon-electron wave vector k-space (2.8 < k < 17.2 Å^{-1}), and subsequently Fourier-transformed into the direct R-space (1.0 < R < 3.8 Å) using the Artemis program from IFEFFIT package [33] and fitted to the EXAFS function [28]. The backscattering amplitudes and phase functions, and the photoelectron free path were theoretically generated from the FEFF6 code.
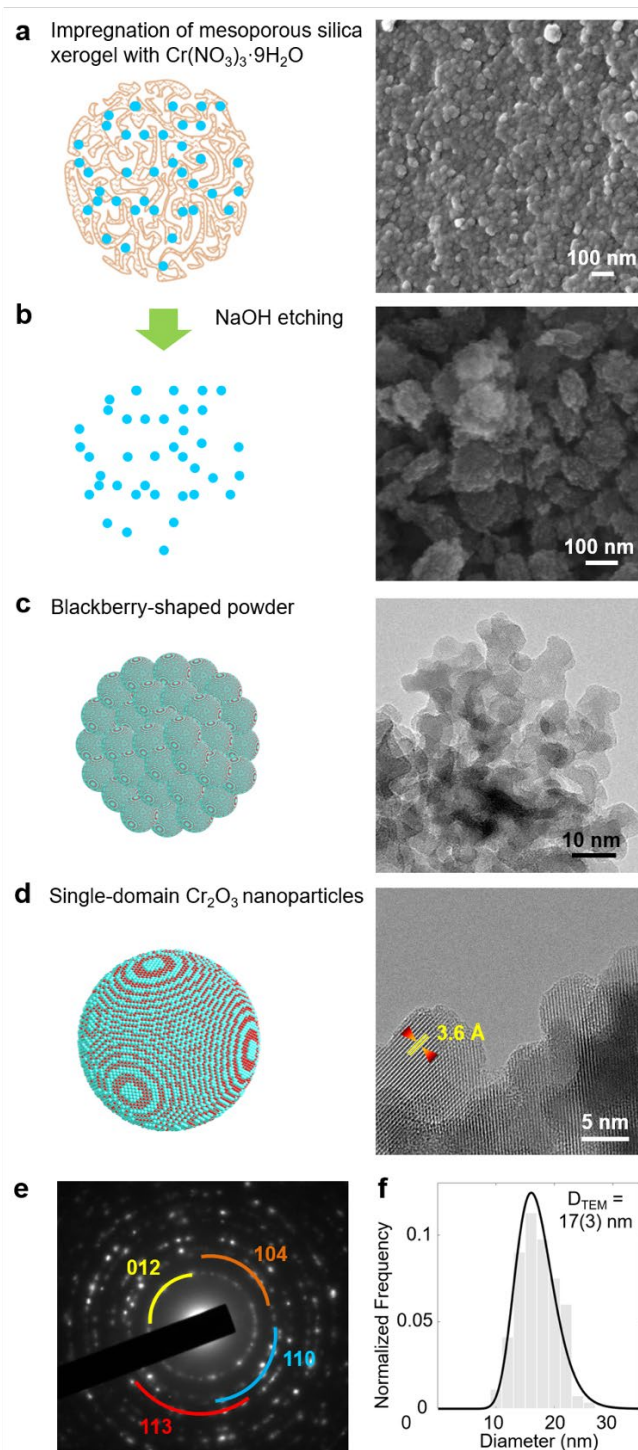

Fig. 1 Synthesis and morphology of the Cr_2O_3 nanoparticles. (a-b) Schematic (left) and scanning electron microscopy micrographs (right) of Cr_2O_3 nucleation and growth within a mesoporous silica template and subsequent NaOH etching. (c-d) Pictures (left) and high-resolution transmission electron microscopy images (right) of the blackberry-shaped powders formed by individual single-domain Cr_2O_3 nanoparticles. The (012) interplanar distance is highlighted. (e) Selected-area electron diffraction (SAED) pattern showing the first four strongest Bragg diffraction rings [(012), (104), (110) and (113)] corresponding to a corundum-type (R-3c) crystal structure (see text for more details). (f) Size histograms as determined from HRTEM measurements, along with a fit to lognormal distribution.

Neutron diffraction (ND) experiments were carried out on a two-axis powder diffractometer (D1B instrument) equipped with a high efficiency position sensitive detector located at the Institut Laue-Langevin (Grenoble, France). ND patterns in a q range of 0.9-4.5 Å^{-1} were collected at various temperatures between 10 K and 330 K using a neutron wavelength of l = 2.52 Å. A double-walled vanadium cylinder sample holder was used to reduce neutron absorption as much as possible. $Al_2Ca_3F_{14}Na_2$ and Si standard samples were measured for determining instrumental resolution and the accurate value of the neutron wavelength. Microstructural analysis based in the parameters used during the Rietveld refinement were performed. The fit was carried out using a Thompson-Cox-Hasting function for the describing the shape of the diffraction peaks, allowing the calculation of both the particle size and strain using a generalized Scherrer peak broadening formula [see reference 34 for more details]. These values were obtained for each individual Bragg reflection both in the paramagnetic and the ordered phase to consider eventual anisotropic broadening in both structural and magnetic contributions. The analysis of the ND data was performed using the FullProf suite package [31].

X-ray magnetic circular dichroism (XMCD) spectra of the Cr_2O_3 NPs spread onto carbon tape were measured on the Boreas beamline (BL 29) at the CELLS-ALBA synchrotron radiation facility (Barcelona, Spain).

The XMCD signal was obtained by combining absorption spectra at the Cr $L_{2,3}$ edges recorded with left and right circularly polarized lights in a magnetic field intensity of 6 T at T = 3 K using the total electron yield method.

The dc magnetic properties of the Cr_2O_3 NPs were studied using a Quantum Design PPMS-14T magnetometer equipped with the VSM option. The magnetization versus temperature measurements were performed in zero-field-cooling (ZFC) and field-cooling (FC) conditions under an applied magnetic field of 10 Oe. Hysteresis loops ($H = \pm$ 60 kOe) after field-cooling the sample (H_{cool} = 10 kOe) from room temperature were recorded at various selected temperatures ranging from 2 to 300 K. The exchange bias field (H_{EB}) is defined as the horizontal shift of the central point of the hysteresis loop measured after field-cooling, i.e., $H_{EB} = (|H_{C2}| - |H_{C1}|)/2$, where H_{C1} and H_{C2} are the left and right coercive fields, respectively. The average coercive field (H_{C-FC}) is defined as $H_{C-FC} = (|H_{C1}| + |H_{C2}|)/2$.

The ac magnetic response of the NPs was measured on a Quantum Design PPMS-14T magnetometer using the ACMS option after ZFC protocol. The real (χ') and imaginary (χ'') parts of the ac magnetic susceptibility were measured on heating from 5 to 300 K under a probing ac magnetic field of 10 Oe in amplitude for different frequencies ($\omega/2\pi$) ranging from 100 to 10000 Hz.

Radio-frequency TS measurements were conducted using a self-resonant tunnel diode oscillator (TDO) with resonant frequency (f) of ~ 12 MHz and sensitivity in the order of 10 Hz [35]. The TDO system is housed outside of a commercial Quantum Design PPMS-9T magnetometer that is used to modulate the applied dc magnetic field as well as the temperature. The sample is placed in the inductive coil of the tank circuit, which is integrated into the PPMS so that the perturbing radio frequency

magnetic field inside the coil (< 10 Oe) is oriented perpendicular to that of the superconducting magnet. As the dc magnetic field or the temperature is varied, the inductance of the coil changes, which causes a shift of the resonant frequency by Δf. The relative change in f provides a direct measure of the TS variation ($\Delta \chi_T$), which is given by:

$$\frac{\Delta f}{f} \propto \left(\frac{\Delta \chi_T}{\chi_T}\right)\% = \frac{|\chi_T(H) - \chi_T^{max}|}{\chi_T^{max}} \times 100$$

Where χ_T^{max} and $\chi_T(H)$ are the maximum value of the TS and the TS at a given magnetic field H, respectively. In a typical measurement procedure, the sample is cooled down to a given temperature in ZFC conditions and then the magnetic field is swept from $+H_{max}$ (= 50 kOe) to $-H_{max}$ (unipolar scan; descending branch) and back to $+H_{max}$ for a bipolar scan (ascending branch).

Results and discussion

Crystal structure, microstructure, and morphology

Insight into the crystallinity of the NPs is provided through SAED image (see Fig. 1e); in this image up to 12 Bragg diffraction rings are detected that correspond to Miller indices (012), (104), (110), (006) (113), (202), (024), (116), (211), (018), (122) and (214), although only the first four rings are labelled in the image for the sake of clarity), and also XRD (see Fig. 2a). The observed Bragg reflections can be indexed according to the same corundum-type crystal structure as hematite (α-Fe_2O_3), described in terms of a hexagonal R-$3c$ unit cell, space group No. 167 (Fig. 2c). Both the lattice parameters, a = 4.951(1) Å and c = 13.590(1) Å, and the adjustable coordinate positions, z_{Cr} = 0.346(1) Å and x_O = 0.309(1) Å, coincide with those obtained for bulk Cr_2O_3 (Fig. 2b) [36].

In order to study how symmetry breaking at the NP surface affects the local structural environment of chromium ions, EXAFS measurements were performed at the Cr K edge (E_0 = 5989 eV) (see Fig. 2d for the k^3-weighted c(k) experimental EXAFS spectra). After Fourier-transforming the EXAFS signals to radial units (R), a satisfactory agreement between experimental data and fit (solid lines in Fig. 2e) is achieved by including in the calculation the single-scattering paths corresponding to O-1, O-2, Cr-1, Cr-2, Cr-3 and Cr-4 neighbouring shells [bottom part of Fig. 2e]. As we move more than ~ 3 Å away from the central atom (Cr-3 and Cr-4 shells), the coordination numbers (N) are noticeably reduced with respect to bulk values (N_{bulk}) (inset in Fig. 2e). This is because surface Cr atoms are under coordinated and that the recorded EXAFS signal is the average over all the Cr absorbing centres. However, in the present case the size of the NPs is large enough so that the decrease of the N/N_{bulk} ratio cannot be detected in the closest coordination shells, but this feature could affect to both the core and shell magnetic structures (see below).

Cr_2O_3 nanoparticle's magnetic structure

We used unpolarized ND experiments to probe the magnetic structure of the Cr_2O_3 NPs. The two ND patterns collected above (300 K) and below (10 K) the magnetic phase transition (270 K)

of Cr_2O_3 are shown in Fig. 3a. First, for T = 300 K, the diffraction pattern can be fitted according to the same corundum-type crystal structure used above for the analysis of the XRD data [36]. Second, on cooling down to T = 10 K, a set of magnetic reflections arises (Fig. 3b), corresponding to an AFM structure with a magnetic propagation vector k = (0,0,0) referred to the crystallographic unit cell [36].

The full-profile fitting of the low temperature pattern indicates that the magnetic moments are collinear and oriented along the c axis following the {+ − + −} stacking sequence (Fig. 3c), this magnetic structure being in good agreement with that earlier reported [37]. Apart from that due to finite size of the NPs, both lattice and magnetic diffraction peaks were broadened commensurate with the particle size. Using the procedure based on a generalized Scherrer-peak-broadening formula [34], it was possible to extract the corresponding sizes of the coherent diffraction domains associated with the peaks related to the crystalline and magnetic structure. It is worth noting the observed remarkable difference between the average diameter of the magnetic (D_{AFM}) and structural (D_{nucl}) coherence domains. While D_{nucl} is similar to the mean NP size derived from transmission electron images [17(1) nm], D_{AFM} is 4 nm smaller [13(1) nm]. The latter suggests a core-shell morphology (see below), which is also consistent with the analysis of the Cr K-edge extended x-ray absorption fine structure (EXAFS) spectra

that indicate the existence of two distinct Cr atomic environments (see Fig. 2d). Moreover, the Fourier Transforms (FT) of the EXAFS signal show almost identical bond distances between NPs and bulk Cr_2O_3, although the Cr coordination number is reduced for R > 3 Å in the NPs (see Fig. 2e). This reduced coordination is expected to occur at the NP shell where the symmetry is partially lost [28].

On the other hand, ND also reveals very significant changes in the magnetic order of the NPs with respect to that of bulk Cr_2O_3. The temperature dependence of the magnetic moment per Cr atom (μ) for Cr_2O_3 NPs was obtained from the refinement of neutron diffraction patterns below the Néel temperature.

This magnetic moment follows a phenomenological expression [38]: $\mu(T) = \mu(0)\,[1-(T/T_N)^{\alpha_1}]^{\alpha_2}$ (see Fig. 3d), where the values for α_1 = 2 and α_2 = 0.33, correspond to the exponents predicted by spin-wave theory for AFM and by the 3D Heisenberg model, respectively [38].

From the temperature dependence of the magnetic moment, $\mu(T)$ curves, there are two important aspects that deserve to be discussed; (i) the magnetic ordering temperature (T_N) of Cr_2O_3 NPs is also reduced relative to the bulk oxide, from 307(2) to 270(7) K owing to finite-size effects on the exchange interactions [39]; and (ii) the value of $\mu(0)$ decreases from 2.56(2) to 1.82(3) μ_B in the NPs.
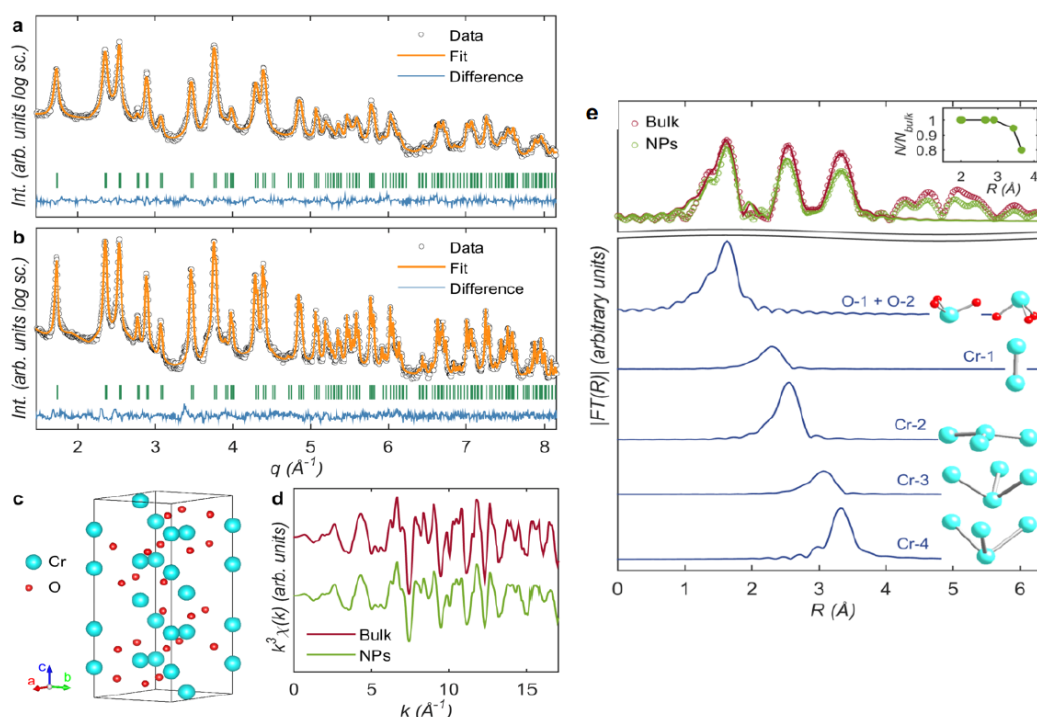
The latter reduction of the magnetic moment per Cr atom could be attributed to the appearance of a spin canting component perpendicular to the AFM axis (see below). Therefore, these findings suggest a progressive loss of AFM order within a ~2 nm-thick shell, and although the NP core retains an AFM arrangement, this order is affected when approaching to the shell due to finite size and interface effects, as already reported for other NP systems of transition metal oxides, such as NiO [28, 29].

Magnetic measurements

In order to disentangle this exotic magnetic scenario, we have measured the temperature dependence of the magnetization in dc and ac conditions.
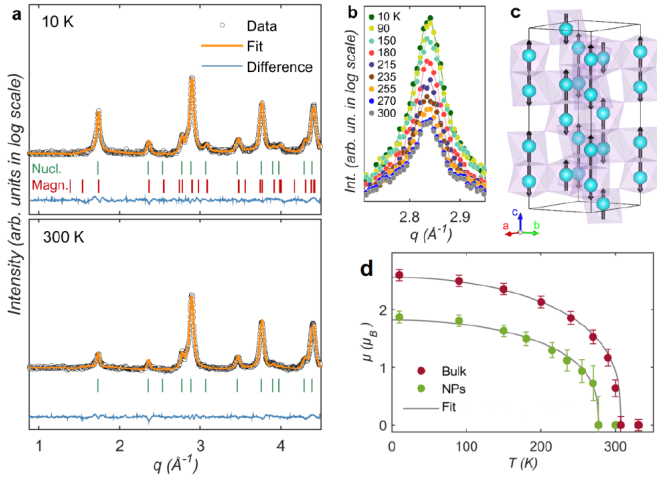
Fig. 3 Magnetic structure and undercoordination of surface Cr atoms. (a) Neutron diffraction patterns in logarithmic vertical scale for Cr_2O_3 NPs for T = 10 K (top) and T = 300 K (bottom). Green and red vertical marks indicate the position of the nuclear and magnetic Bragg reflections, respectively. (b) Temperature dependence of the (012) magnetic reflection for Cr_2O_3 NPs. (c) Hexagonal magnetic unit cell of Cr_2O_3. (d) Temperature dependence of the Cr magnetic moment obtained from ND measurements, together with their fits (see text for details).

The splitting between M_{ZFC} and M_{FC} curves starts at around a temperature close to T_N (inset in Fig. 4a). Deeper insights into the nature of the two M_{ZFC} maxima can be obtained through ac susceptibility (χ) measurements. On the other hand, Figs. 4b-e display the temperature dependence of the real (χ') and imaginary (χ'') parts of χ.

The frequency-independent behaviour of the high-temperature $\chi(T)$ peak (at $T \approx 270$ K, see Figs. 4c and 4e), together with ND results, indicates that this maximum is associated with the T_N of the AFM Cr_2O_3 core. In contrast, the low-temperature peak shifts to higher temperatures on increasing the frequency from

100 to 10000 Hz. This shift is usually quantified as $\Omega = \Delta T / T \log_{10}f = 0.04(1)$, which lies within the range reported for SG-like systems ($0.004 < \Omega_{SG} < 0.06$) [40].
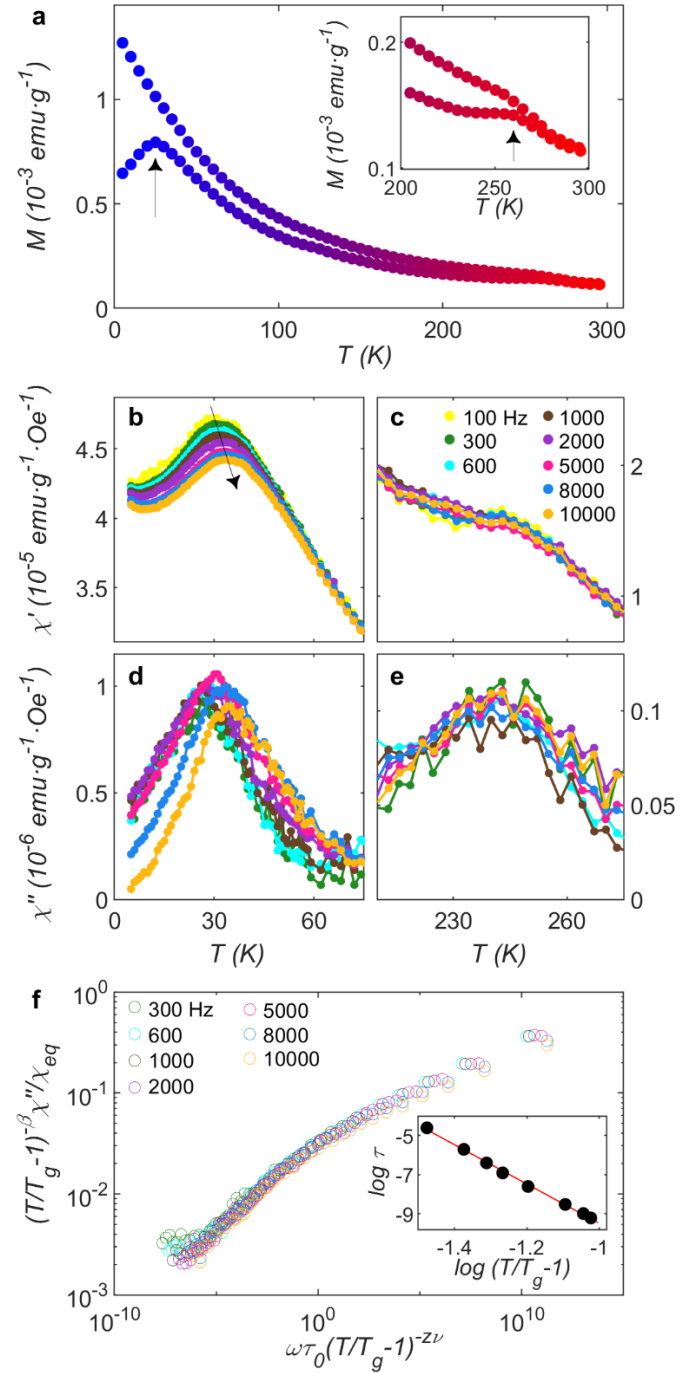

Fig. 4. Temperature dependence of the magnetization measured in dc and ac conditions. (a)M/H curves for Cr_2O_3 NPs under an applied magnetic field of 10 Oe following ZFC and FC procedures. Inset displays an enlarged view of the reversible region ($T > T_N$). Arrows indicate peaks at T~25 K and ~270 K (see text). Temperature dependence of the real (χ') (**b,c**) and imaginary (χ'') (**d,e**) components of the ac susceptibility for different frequencies ranging from 100 to 10000 Hz. (**f**) Dynamic scaling plots obtained from ac susceptibility measurements. Inset shows the best fit of the temperature variation of the low-temperature maximum of χ'' to a critical-slowing-down law. (See text for details).

Assuming that the entities participating in the freezing follow a critical slowing down, the measuring time ($\tau = 1/f$) can be described by the scaling law [41, 42]:

$$\tau = \tau_0 \left(T/T_g - 1\right)^{-z\nu}$$

where $\tau_0 = 10^{-8(1)}$ s is the characteristic relaxation time, $T_g = 25(2)$ K is the glass freezing temperature and $z\nu = 9.8(2)$ is the dynamic exponent (inset in Fig. 4f). In addition, the dynamical critical scaling behaviour of χ'' is also proven by the overlap of the scaled plots of $(T/T_g - 1)^{-\beta} \chi'' / \chi_{eq}$ vs. $\omega\tau_0 (T/T_g - 1)^{-z\nu}$, where $\beta = 0.9(1)$ is a critical exponent, χ_{eq} is the equilibrium susceptibility, obtained from the Curie-Weiss fit of the χ' ($f = 100$ Hz) curve in the 50 K $< T <$ 185 K interval, and $\omega = 2\pi f$ (see Fig. 4f) [43]. Therefore, the magnetic contribution at low temperature ($T < 25$ K) can be attributed to a cluster SG-like collective freezing of the uncompensated spin regions located in the shell layer of the Cr_2O_3 NPs. The obtained values for the fitting parameters τ_0 and $z\nu$ are quite similar to those previously found for NiO NPs that show a similar low-temperature SG-like behaviour, the values being closer to those reported for Ising-type SG-like systems [44, 45]

Moreover, the isothermal magnetization curves, $M(H)$, at different temperatures (see Fig. 7a later), reveal the existence of a non-compensated magnetic signal that disappears at $\sim T_N$ together with the AFM order, indicating a strong coupling between these two types of magnetic orderings. In fact, XMCD measurements are sensitive to differences in the density of empty states with different magnetic spins. The Cr $L_{2,3}$-edge XMCD spectra measured for Cr_2O_3 NPs at 3 K and under an applied magnetic field of 6 T is displayed in Fig. 5. Both $L_{2,3}$ spectral profiles consist of a main negative peak centred at around 577 eV and a smaller positive peak around 578 eV.

This XMCD signal is very small when compared with that found in standard ferromagnetic rare-earth-transition-metal intermetallic compounds [46, 47] though showing similar behaviour and thus indicating that the nature of the magnetic signal is coming from a weak ferromagnetic contribution in Cr_2O_3 NPs. As we will see later, there are two possible sources for this weak ferromagnetic contribution. One of them is related to a non-collinear Canted Magnetic Structure (CMS) at the boundary of the AFM core. The other one is associated with the contribution of short-range weakly interacting regions of pinned uncompensated spins that are randomly disordered at the shell of the NP and collective freeze in a SG-like state at low temperature.

In fact, the nature of this weak ferromagnetism and its temperature evolution is clearly supported by radio-frequency TS measurements, which are sensitive to subtle changes in systems with multiple and competing magnetic orderings, such as NPs with a core-shell morphology [35].
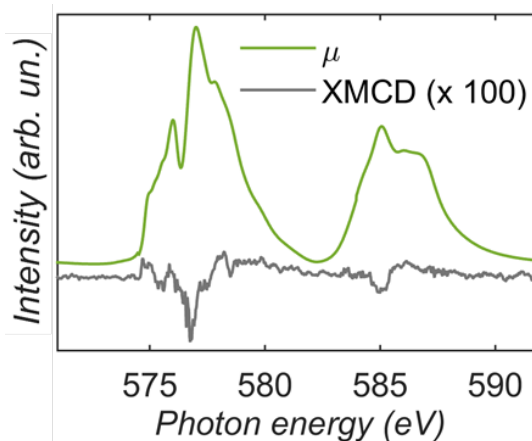

Fig. 5 Low-temperature x-ray magnetic circular dichroism. X-ray absorption (μ) and x-ray magnetic circular dichroism (XMCD) spectra measured at $T = 3$ K under a 6 T magnetic field at the Cr $L_{2,3}$ edges for Cr_2O_3 NPs. The XMCD signal is displayed in percentage and its baseline has been shifted down for the sake of clarity.

It is worth noting that in the ascending branches of the dipolar TS scans (Fig. 6c), the same two anisotropy peaks are observed, but with inverted signs ($-H_{K1}$, H_{K2}) (Fig. 6d). Whereas H_{K1} is normally associated with the effective anisotropy field, $-H_{K2}$ is related to a combination of anisotropy and switching fields on the magnetic moments inside the NP. For a typical ferromagnet, the intensity of $-H_{K2}$ is higher than that of H_{K1}, contrary with what we observe in our Cr_2O_3 NPs. A possible explanation for this is that, by applying a positive magnetic field, we are aligning some canted spins in the direction of the applied magnetic field and, when reversing this field, these spins easily realign if the temperature is high enough. As a result, and according to previous studies [50], the shell of our NPs could be formed by short-range weakly interacting regions of canted spins, whose collective cluster SG-like behaviour is revealed by ac magnetic susceptibility measurements (see Fig. 4) as mentioned before.

This idea is further supported by Fig. 6e, which shows the temperature evolution of H_{K1}, H_{K2}, $-H_{K1}$ and $-H_{K2}$. At $T = T_N$, the two anisotropy peaks merge into a single one, indicating that the entire system is in a paramagnetic state. On cooling down from $T = T_N$, H_{K1} and $-H_{K2}$ display a similar trend (despite the different sign), but for $T<T_g$ the slope of $-H_{K2}$ vs. T changes abruptly. This feature suggests that the interaction between non collinear weak ferromagnetic regions favour their realignment as the temperature decreases, thus provoking a non-smooth evolution of the effective anisotropy. Moreover, the collective freezing of the spin-canted regions results in a steep increase of the anisotropy field below around $T = 25$ K.
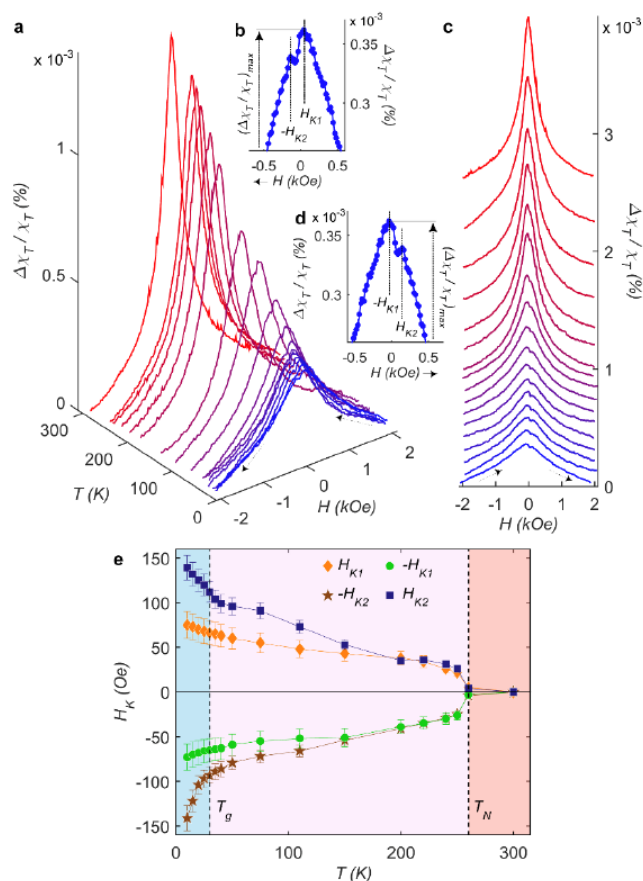
Fig. 6 Effective anisotropy and radio frequency transverse susceptibility (TS) measurements. (a) 3D plot of the temperature (T = 10, 15, 20, 25, 30, 35, 40, 50, 75, 110, 150, 200, 220, 240, 250, 260 and 300 K) and magnetic field dependences of the TS (the magnetic field is varied from positive to negative values, descending branch). (b) Representative unipolar descending TS scan at T = 10 K that illustrates the position of the anisotropy peaks and the maximum value of $\Delta\chi_T/\chi_T$. (c) Temperature dependence of TS measured under a magnetic field varying from negative to positive values (ascending branch). (d) Representative unipolar ascending TS scan at T = 10 K, showing the inversion of the anisotropy peaks with respect to (b). (e) Temperature dependence of the anisotropy fields extracted from the descending (H_{K1}, $-H_{K2}$) and ascending ($-H_{K1}$, H_{K2}) TS branches.

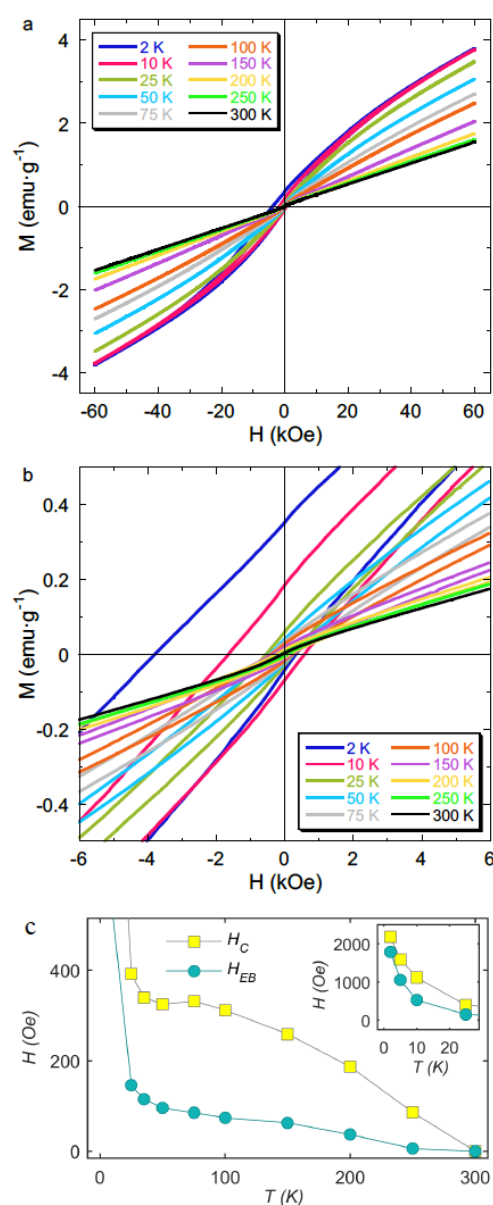**Core-shell exchange bias interaction**

Fig. 7 Magnetization curves and exchange bias effect. (a) $M(H)$ curves for Cr_2O_3 nanoparticles, measured at different temperatures after cooling the sample from room temperature under a magnetic field H_{cool} = 10 kOe (b); Central region of the magnetization vs. magnetic field curves measured after fied-cooling (H_{cool} = 10 kOe) from room temperature; (c) Temperature dependences of the coercive and exchange bias fields. Inset shows an enlarged view of the low temperature region. Lines provide guides for the eyes (see text for details).

The temperature dependence of the EB (H_{EB}) and coercive (H_C) fields are displayed in Fig. 7c. Unlike a vast majority of exchange-bias systems [53], both H_{EB} and H_C persist up to T_N owing to the fact that the net magnetization at the boundary is coupled to the core antiferromagnetic order parameter [51], which is consistent with our picture of an AFM core intimately connected to a shell of canted magnetic moments.

effect below 25 K coming from the CMS/SG interface coupling. This feature means that the freezing of spins in this outer layer below 25 K strongly impacts the ordering of canted spins within the weak ferromagnetic interface. Similar to that already observed in NiO nanoparticles, with a core-shell morphology where the EB effect was attributed to the SG-shell. In this NP-NiO system the EB effect is present up to the freezing temperature (< 150 K) of the SG-shell, well below the T_N of NiO (523 K) [29]. In addition, at low temperatures (~ 10 K) the coercive field in NiO NPs is smaller than that of Cr_2O_3 NPs because the exchange bias at the AFM/CMS interface is in grand part affected by the behaviour of canted and pinned uncompensated spins. In fact, in the temperature range 25 < T < 270 K, the outer shell spins are unfrozen, so their impact on the SG layer is almost negligible. This explains why H_K increases gradually with decreasing temperature in this temperature range. Below 25 K spins within the outer shell are frozen, so their impact is much more significant, resulting in the sharp increase in H_K. In addition, interparticle interactions between the NPs might become stronger at $T < T_g$, giving rise to the enhanced H_K in this temperature region.

The simultaneous observation of hysteresis loop broadening and shift in an EB system comprising a thin canted magnetic structure and a thicker AFM could be interpreted as the formation of an entangled exchange core/shell across the AFM material [29, 54]. On these grounds, an eventual magnetic-field-induced rotation of the canted magnetic component at the boundary of the core could severely torque the orientation of the core magnetic moments several nm inside the NP core (up to 10 nm in some cases [49]). Remarkably, the effect of this exchange coupling is gradual, and it monotonically fades away from the interface.

On the other hand, it is worth noting that the dipolar dipole-dipole interactions and exchange interactions might be quite well affected by aggregation or agglomeration processes, commented above [55, 56]. This feature could have a strong impact on the collective magnetic properties of NPs at low temperatures below T_g. However, above this temperature when the spins located at the shell are in a superparamagnetic state this influence is expected to be almost negligible. This point reinforces the idea of an entanglement between the AFM-state of the core spins and the canted spin magnetic structure at the interface coupled to it, the exchange bias being set exactly at the core Néel temperature and persisting up to near room temperature.

The final picture that emerges from the present findings is illustrated in Fig. 8, where a schematic representation of the magnetic arrangements in one-single NP is proposed. Firstly, the core spins adopt the same collinear AFM ordering as that of bulk Cr_2O_3. Next, as commented about, using symmetry arguments, in a magnetoelectric antiferromagnet, such as Cr_2O_3, the system could develop an equilibrium net magnetization at the boundary of the AFM structure (this magnetization is related to the presence of a non collinear ordering in Cr_2O_3 NPs that was evidenced through a transversal or spin canting component with respect to the AFM direction). And then, the existence of disorder at the surface of the NP is responsible for the existence of a short-range weakly interacting spins that collectively freeze in a SG-like state at low temperatures. Relevant issues related to the nature of the magnetic orderings involved in Cr_2O_3 NPs remain unanswered that may be crucial for further investigation.
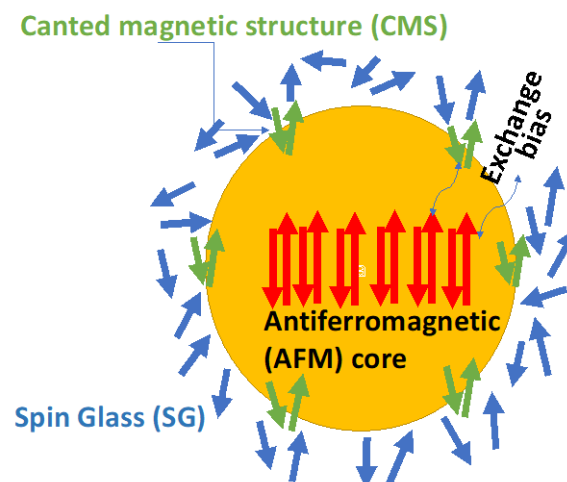

Fig. 8 Low-temperature spatially modulated magnetic structure in Cr_2O_3 NPs. Schematic illustration of the whole NP magnetic structure with a core-shell morphology. The inner NP core retains the AFM order of bulk Cr_2O_3, while a disordered outer shell exhibits canted AFM and SG-like behaviours (see text).

In summary, we have prepared Cr_2O_3 NPs that display a spatially modulated magnetic structure that reflects the transition evolving from an AFM core to a SG shell. Magnetic and structural analyses have revealed that the lattice periodicity breaking at the surface of the NPs plays a crucial role in generating a non-collinear magnetic structure. Quantitative arguments show that the SG arrangement forms a 2 nm thick surface shell and persists magnetically ordered up to near room temperature and vanishes concomitant and entangled to the AFM long range order through the canted magnetic structure at the boundary of the AFM. Furthermore, this intimate coupling between the shell and the AFM core, through the canted magnetic structure at the interface, echoes in a robust exchange bias effect which also disappears precisely at T_N. The features displayed by the exchange-biased magnetic hysteresis could be the object of further future research to elucidate the behaviour of both pinned uncompensated and canted moments in nanoparticle systems with different morphologies and microstructures.

Author Contributions

N. R.-M. performed magnetic measurements, collected HRTEM images and participated in the ND and Synchrotron experiments; she also carried out most of the data analysis and prepared the original

Conflicts of interest

There are no conflicts to declare.

Acknowledgements

Notes and references

1   L. Néel, *C. r. hebd. séances Acad. sci.*, 1947, **224**, 1488.
2   K. Wu, D. Su, J. Liu, R. Saha and J.-P. Wang, *Nanotechnology*, 2019, **30**, 502003.
3   A. Hirohata, K. Yamada, Y. Nakatani, I.-L. Prejbeanu, B. Diény, P. Pirro and B. Hillebrands, *J. Magn. Magn. Mater.*, 2020, **509**, 166711.
4   M. Neamtu, C. Nadejde, V.-D. Hodoroaba, R.J. Schneider, L. Verestiuc and U. Panne, *Sci. Rep.*, 2018, **8**, 6278.
5   D. Halley, N. Najjari, H. Majjad, L. Joly, P. Ohresser, F. Scheurer, C. Ulhaq-Bouillet, S. Berciaud, B. Boudin and Y. Henry, *Nature Comm.*, 2000, **5,** 3167.
6   W. Eerenstein, N.D. Mathur and J.F. Scott, *Nature*, 2006, **442**, 759.
7   R. Ramesh, *Nature Mater.*, 2010, **9**, 380.
8   S. Mu and K.D. Belashchenko, *Phys. Rev. Mat.*, 2019, **3**, 034405.
9   D. Khomskii, *Physics*, 2009, **2**, 20.
10 I. Dzyaloshinskii, *JETP*, 1960, **10**, 628.
11 S.-W. Cheong and M. Mostovoy, *Nature Mater.*, 2007, **6**, 13.
12 M. Mostovoy, A. Scaramucci, N.A. Spaldin and K.T. Delaney, *Phys. Rev. Lett.*, 2010, **105**, 87202.
13 Li. Junxue, B. Wilson, R. Cheng, M. Lohmann, M. Kavand, W. Yuan, M. Aldosary, M. Agladze, P. Wei, M.S. Sherwin and J. Shi, *Nature*, 2020, **578**, 70.
14 G. Hao, L. Xiao, Y. Hu, F. Shao, X. Ke, J. Liu, F. Li, W. Jiang, F. Zhao and H. Gao, *J. Energetic Materials*, 2019, 37, 251.
15 L. Xia, B. Li, Y. Zhang, R. Zhang, L. Ji, H. Chen, G. Cui, H. Zheng, X. Sun, F. Xie and Q. Liu, *Inorganic Chem.*, 2019, 58, 2257.
16 M. Isacfranklin, F. Ameen, G. Ravi, R. Yuvakkumar, S.I. Hong, D. Velauthapillai, M. Thambidurai and C. Dang, *Ceramics International*, 2020, **46**, 19890.
17 G. Susoy, E.E. Altunsoy Guclu, O. Kilicoglu, M. Kamislioglu, M.S. Al-Buriahi, M.M. Abuzaid and H.O. Tekin, *Mat. Chem. Phys.*, 2020, **242**, 122481.
18 A. Iyama and T. Kimura, *Phys. Rev. B*, 2013, **87**, 180408.
19 J.F. Scott, *NPG Asia Mater.*, 2013, **5**, e72.
20 B. Goodenough, Magnetism and the chemical bond (Wiley, New York, USA, 1963).
21 K.N. Trohidou, X. Zianni and J.A. Blackman, *J. Appl. Phys.*, 1998, **84**, 2795.
22 D. Tobia, E. Winkler, R.D. Zysler, M. Granada and H.E. Troiani, *Phys. Rev. B*, 2008, **78**, 104412.
23 M. Bañobre-López, C. Vázquez-Vázquez, J. Rivas and M.A. López-Quintela, *Nanotechnology*, 2003, **14**, 318.
24 D. Li, Z. Han, J.G. Zheng, X.L. Wang, D.Y. Geng, J. Li and Z.D. Zhang, *J. Appl. Phys.*, 2009, **106**, 53913.
25 S. Punugupati, J. Narayan and F. Hunte, *Appl. Phys. Lett.*, 2014, **105**, 132401.
26 A. Ghosh, K. Dey, Sk. Sabyasachi, A. Karmakar, S. Majumdar and S. Giri, *Appl. Phys. Lett.*, 2013, **103**, 52412.
27 E. Winkler, R.D. Zysler, M. Vasquez Mansilla, D. Fiorani, D. Rinaldi, M. Vasilakaki and K.N. Trohidou, *Nanotechnology*, 2008, **19** 185702.
28 N. Rinaldi-Montes, P. Gorria, D. Martinez-Blanco, A.B. Fuertes, L. Fernandez Barquin, J. Rodriguez Fernandez, I. de Pedro, M.L. Fdez-Gubieda, J. Alonso, L. Olivi, G. Aquilanti and J.A. Blanco, *Nanoscale*, 2014, **6**, 457.
29 N. Rinaldi-Montes, P. Gorria, D. Martinez-Blanco, A.B. Fuertes, L. Fernandez Barquin, I. Puente-Orench and J.A. Blanco, *Nanotechnology*, 2015, **26**, 305705.
30 A.B. Fuertes, *J. Phys. Chem. Solids*, 2005, **66**, 741.
31 J. Rodriguez-Carvajal, Fullprof: a program for Rietveld refinement and pattern matching analysis. Satell. Meet. Powder Diffr. XV IUCr Congr. 127, (1990).
32 H. Rietveld, *J. Appl. Crystallogr.*, 1969, **2**, 65.
33 B. Ravel and M. Newville, *J. Synchrotron Radiat.*, 2005, **12**, 537.
34 D. Martínez-Blanco, P. Gorria, J. A. Blanco, M. J. Pérez and J. Campo, *J. Phys.: Condens. Matter*, 2008, **20**, 335213.
35 H. Srikanth, J. Wiggins and H. Rees, *Rev. Sci. Instrum.*, 1999, **70**, 3097.
36 B.N. Brockhouse, *J. Chem. Phys.*, 1953, **21**, 961.
37 L.M. Corliss, J.M. Hastings, R. Nathans and G. Shirane, *J. Appl. Phys.*, 1965, **36**, 1099.
38 V.M.T.S. Barthem, C.V. Colin, H. Mayaffre, M.-H. Julien and D. Givord, *Nature Comm.*, 2013, **4**, 2892.
39 R.H. Kodama, *J. Magn. Magn. Mater.*, 1999, **200**, 359.
40 S. Thota and J. Kumar, *J. Phys. Chem. Solids*, 2007, **68**, 1952.
41 J.A. Mydosh, Spin Glasses: and experimental introduction (Taylor & Francis, London, 1993).
42 F. Fernandez Barquín, J.C. Gómez Sal, P. Gorria, J.S. Garitaonandia and J.M. Barandiarán, *Eur. Phys. J. B*, 2003, **35**, 3.
43 J. Dorman, L. Bessais and D. Fiorani, *J. Phys. C.: Solid State Physics*, 1988, **21**, 2015.
44 T. Nakamura, *Phys. Rev. B*, 2010, **82**, 014427.
45 R.E. Blundell, K. Humayun and A.J. Bray, *J. Phys. A: Math. Gen.*, 1992, **25**, L733.
46 R.M. Galera, S. Pizzini, J.A. Blanco *et al.*, *Phys. Rev. B*, 1995, **51**, 15957.

47 P. Gorria, D. Martinez-Blanco, M.J. Perez *et al.*, *Phys. Rev. B*, 2009, **80**, 064421.
48 A. Aharoni, E.H. Frei, S. Shtrikman and D. Treves, Bull. Res. Counc. Isr., 1957, **6A**, 215.
49 S. Chandra, H. Khurshid, M.-H. Phan and H. Srikanth, Appl. Phys. Lett., 2012, **101**, 232405.
50 S. Chandra, N.A. Frey Huls, M.-H. Phan, S. Srinath, M.A. Garcia, Y. Lee, C. Wang, S. Sun, O. Iglesias and H. Srikanth, Nanotechnology, 2014, **25**, 55702.
51 K.D. Belashchenko, *Phys. Rev. Lett.*, 2010, **105**, 147204.
52 J. Nogues, J. Sort, V. Langlais, V. Skumryev, S. Suriñach, J.S. Muñoz and M.D. Baró, Phys. Rep., 2005, **422**, 65.
53 J. Nogues and I.K. Schuller, J. Magn. Magn. Mater., 1999, **192**, 203.
54 F. Radu and H. Zabel, Exchange bias effect of ferro-/antiferromagnetic heterostructures. In: H. Zabel and S.D. Bader (eds) Magnetic Heterostructures. Springer Tracts in Modern Physics, **227**, 97. (Springer, Berlin, Heidelberg, 2008).
55 L. Gutierrez, L. de la Cueva, M. Moros, E. Mazario, S. de Bernardo, J.M. de la Fuente, M.P. Morales and G. Salas, *Nanotechnology*, 2019, **30**, 112001.
56 X. Batlle, C. Moya, M. Escoda-Torroella, O. Iglesias, A. Fraile Rodríguez and A. Labarta, *J. Magn. Magn. Mater.*, 2022, **543**, 168594.